



# Versatile and automated workflow for the analysis of oligodendroglial calcium signals

Dorien A. Maas<sup>1</sup> · Blandine Manot-Saillet<sup>1</sup> · Philippe Bun<sup>2</sup> · Chloé Habermacher<sup>1,6</sup> · Corinne Poilbout<sup>1</sup> · Filippo Rusconi<sup>4,5</sup> · Maria Cecilia Angulo<sup>1,3</sup>

Received: 2 February 2023 / Revised: 20 November 2023 / Accepted: 27 November 2023 / Published online: 9 January 2024  
© The Author(s), under exclusive licence to Springer Nature Switzerland AG 2024, corrected publication 2024

## Abstract

Although intracellular  $\text{Ca}^{2+}$  signals of oligodendroglia, the myelin-forming cells of the central nervous system, regulate vital cellular processes including myelination, few studies on oligodendroglia  $\text{Ca}^{2+}$  signal dynamics have been carried out and existing software solutions are not adapted to the analysis of the complex  $\text{Ca}^{2+}$  signal characteristics of these cells. Here, we provide a comprehensive solution to analyze oligodendroglia  $\text{Ca}^{2+}$  imaging data at the population and single-cell levels. We describe a new analytical pipeline containing two free, open source and cross-platform software programs, Occam and post-prOccam, that enable the fully automated analysis of one- and two-photon  $\text{Ca}^{2+}$  imaging datasets from oligodendroglia obtained by either ex vivo or in vivo  $\text{Ca}^{2+}$  imaging techniques. Easily configurable, our software solution is optimized to obtain unbiased results from large datasets acquired with different imaging techniques. Compared to other recent software, our solution proved to be fast, low memory demanding and faithful in the analysis of oligodendroglial  $\text{Ca}^{2+}$  signals in all tested imaging conditions. Our versatile and accessible  $\text{Ca}^{2+}$  imaging data analysis tool will facilitate the elucidation of  $\text{Ca}^{2+}$ -mediated mechanisms in oligodendroglia. Its configurability should also ensure its suitability with new use cases such as other glial cell types or even cells outside the CNS.

**Keywords** Oligodendrocytes · Calcium imaging · Microendoscopy · Two-photon microscopy · Open-source · Microscopy data analysis

---

Dorien A. Maas and Blandine Manot-Saillet contributed equally to this work.

---

✉ Maria Cecilia Angulo  
maria-cecilia.angulo@parisdescartes.fr

- <sup>1</sup> Université Paris Cité, Institute of Psychiatry and Neuroscience of Paris (IPNP), INSERM U1266, “Team: Interactions Between Neurons and Oligodendroglia in Myelination and Myelin Repair”, 75014 Paris, France
- <sup>2</sup> Université Paris Cité, Institute of Psychiatry and Neuroscience of Paris (IPNP), INSERM U1266, “NeurImag Platform”, 75014 Paris, France
- <sup>3</sup> GHU PARIS Psychiatrie and Neurosciences, 75014 Paris, France
- <sup>4</sup> IDEEV, GQE, Université Paris-Saclay, CNRS, INRAE, AgroParisTech, 12, Route 128, 91272 Gif-sur-Yvette, France
- <sup>5</sup> Centre de Recherche des Cordeliers, Sorbonne Université, INSERM, Université Paris Cité, 75006 Paris, France
- <sup>6</sup> Present Address: SynapCell, Bâtiment Synergy Zac Isiparc, 38330 Saint Ismier, France

## Introduction

It is now established that  $\text{Ca}^{2+}$  signals of oligodendroglia, the myelinating cells of the central nervous system, convert environmental information to cellular processes such as proliferation, differentiation and myelination [20, 24, 25]. Primary in vivo studies in the zebrafish revealed that both oligodendrocyte precursor cells (OPCs) and oligodendrocytes (OLs) are capable of  $\text{Ca}^{2+}$  signaling [5, 16, 19]. In mouse brain slices, spontaneous  $\text{Ca}^{2+}$  activity in OPCs [4] and OLs [6] is high during postnatal development when the myelination process is still ongoing, and decreases in OLs as the brain matures [6]. Then,  $\text{Ca}^{2+}$  signals of OLs are reactivated upon demyelination in the adult mouse brain, suggesting that they play a crucial role in demyelinated lesions [6]. To date, compared to the large number of reports in other CNS cell types, only few studies have explored ex vivo and in vivo oligodendroglia  $\text{Ca}^{2+}$  signaling under healthy and pathological conditions. Moreover, in the above-mentioned studies, not only were

the regions of interest (ROIs) manually chosen, potentially introducing bias in the ROI selection outcome, but also complex  $\text{Ca}^{2+}$  events with multiple peaks were overlooked even though these events are a hallmark of both OPCs and OLs (see below).

Several software pipelines for the analysis of  $\text{Ca}^{2+}$  imaging data from both neurons and astrocytes, in brain slices and in vivo, have been published. Unfortunately, problems arise when using neuron-oriented programs such as CaImAn and EZCalcium for the analysis of oligodendroglial  $\text{Ca}^{2+}$  imaging data [8, 12]. For instance, classifiers are used to recognize neurons as round somata of a certain size [12], while oligodendroglia possess less well-defined shapes and sizes [32]. Another important drawback of the available pipelines for neuronal  $\text{Ca}^{2+}$  imaging is the difference in neuronal and oligodendroglial  $\text{Ca}^{2+}$  signal dynamics. Indeed, neuronal  $\text{Ca}^{2+}$  signals last around 100 ms, are characterized by fast kinetics and occur with a high frequency [9]. This is in stark contrast with OLs that exhibit complex  $\text{Ca}^{2+}$  dynamics, with signals that last anywhere from several seconds to multiple minutes and that are characterized by slow rise and decay times (our data and [6]. Another set of problems may arise when using available  $\text{Ca}^{2+}$  imaging analysis for astrocytes in OL lineage cells: astrocytes are known to exhibit extensive signal propagation within and between cells and  $\text{Ca}^{2+}$  signaling software pipelines such as AQuA are, therefore, designed to trace  $\text{Ca}^{2+}$  events in time and space instead of identifying ROIs [30]. Since we cannot assume that intra- and inter-cellular signal propagation occurs extensively in OPCs and OLs, these software pipelines are not readily suitable for the analysis of oligodendroglial  $\text{Ca}^{2+}$  signaling. Other ROI-based astrocyte  $\text{Ca}^{2+}$  imaging analysis packages, such as GECIquant and CaSCaDe, are semi-automated, which may introduce bias making them less desirable [2, 29] or, such as Begonia, are optimized for two-photon microscopy limiting the use to this imaging modality [7].

Here, we provide a comprehensive analytical pipeline-based package to explore oligodendroglial  $\text{Ca}^{2+}$  imaging data obtained either ex vivo or in vivo. We developed two Free Open Source cross-platform software programs, Occam and post-prOccam (Occam: Oligodendroglial cells calcium activity monitoring; post-prOccam: post-processing of the data first output by Occam), for the fully automated analysis of one- and two-photon  $\text{Ca}^{2+}$  imaging data from OPCs and OLs (GNU GPLv3 + license; code repository at: <https://gitlab.com/d5674/occam>). These highly versatile and accessible tools are suitable for the analysis of  $\text{Ca}^{2+}$  imaging datasets obtained with different imaging techniques and in diverse preparations, matching the specific requirements for the monitoring of the complex  $\text{Ca}^{2+}$  event characteristics observed in OL lineage cells. Our software should accelerate the elucidation of  $\text{Ca}^{2+}$ -mediated mechanisms in oligodendroglia and might contribute to the development

of therapeutic strategies in myelin-related disorders such as multiple sclerosis.

## Materials and methods

### Experimental animals

All the experiments followed European Union and institutional guidelines for the care and use of laboratory animals and were approved by both the French ethical committee for animal care of the University Paris Cité (Paris, France) and the Ministry of National Education and Research (Authorization N° 13093-2017081713462292). They were performed with male and female *Pdgfra*<sup>CreERT(±)</sup>;*Gcamp6f*<sup>Lox/Lox</sup> or *Pdgfra*<sup>CreERT(±)</sup>;*Gcamp5-tdTomato*<sup>Lox/Lox</sup> transgenic adult mice (7 to 9 weeks old) obtained by crossing *Pdgfra*<sup>CreERT</sup> (stock 018280, The Jackson Laboratory) with *Ai95(Rcl-Gcamp6f)-D* (stock 028865, The Jackson Laboratory, USA) or *Gcamp5-tdTomato*<sup>Lox/Lox</sup> (stock 028865, The Jackson Laboratory, USA). Animals were genotyped by PCR using specific primers for Cre. All animals had ad libitum access to food and water and were exposed to a 12-h light/dark cycle, a controlled average temperature of 21 °C and 45% humidity (see Supplementary Materials and Methods for details on experimental procedures on slice preparation and demyelinated lesions).

### Ex vivo wide-field calcium imaging

Cells expressing GCaMP6f in acute slices containing LPC-induced demyelinated lesions of corpus callosum were visualized with a 40× water-immersion objective in a wide-field microscope (NA: 0.80, Olympus BX51) using a LED system (CoolLED PE-2; Scientifica, UK) and a CCD camera (ImageQ, Optimos; Scientifica, UK) (Supplementary Materials and Methods [21]). Excitation and emission wavelengths were obtained using 470 nm and 525 nm filters, respectively (Ref: 49,002; Chroma, USA). The CCD camera and the LED system were controlled using a Digidata 1440A interface and Pclamp10.5 software (Molecular Devices, USA). The image stacks were acquired at a frame rate of 1.75 Hz with 50 ms light exposure for a total duration of 240 s using Micro-manager-1.4 plugin under the Fiji/ImageJ2 framework (version 1.53 k or later) [27]. In few cases, we observed GcaMP6f<sup>+</sup> vascular cells in demyelinated lesions at 7 days post-LPC injections (dpi), i.e., 2 weeks after the first tamoxifen injection (50 mg/kg per injection; Supplementary Fig. 1d), that may correspond to PDGFR $\alpha$ -expressing perivascular fibroblasts. Easily identified by their vascular shape, we could discard the fields containing these cells during the experiment or the analysis.  $\text{Ca}^{2+}$  imaging during bath applications of 50  $\mu\text{M}$  carbachol were performed after incubating the

slices for five minutes with an antagonist cocktail containing 10  $\mu\text{M}$  NBQX, 50  $\mu\text{M}$  AP5, 10  $\mu\text{M}$  GABA<sub>A</sub>zine, 1  $\mu\text{M}$  TTX and 50  $\mu\text{M}$  mecamylamine.

### Ex vivo two-photon calcium imaging

Two-photon  $\text{Ca}^{2+}$  imaging of putative GCaMP5<sup>+</sup> OPCs and OLs in acute slices of LPC-induced demyelinated lesions of corpus callosum was performed using a two-photon laser scanning microscope and acquired in frame mode (150–250 ms per frame) with custom-made software (LabVIEW, National Instruments) as previously described [4, 23]. Briefly, a 40 $\times$  water-immersion objective (Olympus40x LumPlanFL N 540x/0.8) in combination with a 900 nm excitation beam from a femtosecond Ti:Sapphire laser (10 W pump; Mira 900 Coherent, Santa Clara, CA) was used to image GcaMP5 in areas sized 1148–2000  $\mu\text{m}^2$ . GcaMP5 was detected with Hamamatsu photon counting PMTs through an emission filter (HQ500/40, Chroma). Pixel dwell time was fixed at 6.2  $\mu\text{s}$ .  $\text{Ca}^{2+}$  signals of individual cells were imaged at 3.60–6.27 frames per second during 99 s. To distinguish OPCs and OLs, we used morphological criteria and recorded only cells for which we could connect the processes to a particular soma. In corpus callosum, OPCs were characterized by a relatively small round soma and a stellate arborization with thin processes, whereas OLs had a larger soma and principal processes often aligned with axons.

### Occam and post-prOccam: $\text{Ca}^{2+}$ signal analysis software programs for the investigation of oligodendroglia

The imaging data analysis is performed in two steps by the two distinct software pieces thoroughly described in “Results” and in the software user manual provided as supplementary information (Supplementary manual). Briefly, the Occam program first processes the image stack producing data stored in a set of files that are then processed by the post-prOccam program for data refinement and statistical calculations. Occam is a Fiji/ImageJ2-based plugin written in Java (Fiji/Imagej2 framework version 1.53 k or later) and post-prOccam is written in Python3. One important feature of our software package is that both Occam and post-prOccam can be extensively configured to adapt the processing to ex vivo wide-field, ex vivo two-photon or in vivo microendoscopic  $\text{Ca}^{2+}$  imaging stacks. The configuration allows for an optimized processing of the  $\text{Ca}^{2+}$  signals acquired in these different preparations (see configuration file examples for each condition in Supplementary Files 1–3; Supplementary manual). The software described in this report is cross-platform Free and Open Source Software (FOSS) and licensed under the GNU GPLv3 + license (code and documentation are available at: <https://gitlab.com/d5674/occam>).

### Benchmarking two other software offerings against Occam/post-prOccam

Our software package was benchmarked against other available software. To this end, all of our datasets used in this study were reanalyzed with GECIquant and AQuA, two programs running under the same Fiji/ImageJ2 framework [29, 30]. To minimize the comparison bias, all the user-settable parameters were optimally tuned for each tested program in each imaging condition. All the comparisons of the three software programs were performed with the same parameters of spatial and temporal resolution (pixel size, acquisition rate) and minimal pixel size (300 pixels for ex vivo wide-field, 20 pixels for ex vivo two-photon microscopy, 80 pixels for in vivo microendoscopy). The benchmark was run on a computer under the Debian GNU/Linux version 11 operating system (DELL Latitude, Intel(R) Xeon(R), CPU E3-1505 M v6 at 3.00 GHz, 4 cores, Graphics NVIDIA Quadro M1200, 32 Gb RAM). For AQuA, additional parameters were set as follows: intensity threshold scaling factor: 5, for ex vivo wide-field; 2–3, for ex vivo two-photon microscopy and 2–3, for in vivo microendoscopy; smoothing: 1; temporal cut threshold: 3; growing z threshold: 1; rising time uncertainty: 2; slowest delay in propagation: 1; propagation smoothness: 1; Z score threshold: 2.

### Automated analysis of $\text{Ca}^{2+}$ signals from OPCs, OLs and myelin sheaths in different species and imaging conditions

Our software package was tested on datasets from OPCs, OLs and myelin sheaths acquired using one-photon or two-photon microscopy in different laboratories. Since these images were acquired at different magnifications and in different microscopy setups, we trained WEKA plugin separately with each image stack to generate specific classifiers. Then, we proceeded to the automated analysis with Occam by setting a minimal pixel size at 20, except for OPCs in zebrafish for which we used a minimal pixel size of 10. Occam was configured as ex vivo two-photon microscopy for cells recorded in mouse preparations and zebrafish myelin processes in zebrafish and in vivo wide-field for OPCs in zebrafish. The other parameters were set as default values in mouse preparations. For zebrafish, we used a spatial binning value of 2 for myelin sheaths and the following parameters for OPCs: overlap: 30%, binning value 1, temporal trimming value 12, spatial trimming value 40, number of frames in the substack: 2. For each analyzed image stack, the parameters in the configuration file used by post-prOccam were set according to the acquisition rate and the area of the images and adjusted according to the recording conditions and noise. ROI trace correction was always performed using  $\Delta F/F$ .

## Statistical analysis

Data are expressed as mean  $\pm$  SEM. GraphPad Prism (version 9.3.0; GraphPad Software Inc., USA) was used for statistical analysis. Each group of data was first subjected to Shapiro–Wilk normality test. According to the data structure, two-group comparisons were performed using the two-tailed unpaired Student's *t*-test or the non-parametric two-tailed unpaired Mann–Whitney *U* test for independent samples; the two-tailed paired Student's *t*-test was used for paired samples. Multiple comparisons were done with a one-way ANOVA test followed by a Tukey's multiple comparison test, the non-parametric Friedman test followed by a Dunn's multiple comparison test or the two-way ANOVA test followed by a Bonferroni's multiple comparison test.

## Results

### Occam performs automated noise correction and ROI definition

The goal of this study was to develop a fully automated analytical workflow for the investigation of one- and two-photon intracellular Ca<sup>2+</sup> imaging data from OPCs and OLs in ex vivo and in vivo preparations. We developed the Occam and post-prOccam software programs for this purpose by initially using wide-field Ca<sup>2+</sup> imaging stacks in acute slices obtained in mouse corpus callosum demyelinated lesions. Since in this kind of imaging condition OPCs and OLs expressing cytosolic GCaMP6f are indistinguishable [26], we hereinafter refer to these cells with the generic term oligodendroglia. We later expanded the scope of the software by implementing new features for the analysis of two-photon Ca<sup>2+</sup> imaging stacks of single OPCs and OLs and in vivo microendoscopy Ca<sup>2+</sup> imaging stacks of oligodendroglia using a miniscope (Fig. 1). Our software was initially developed and validated for the processing of imaging data obtained in demyelinated lesions in mouse models where the GCaMP protein is not expressed in OL lineage cells in healthy white matter (*Pdgfra*<sup>CreERT(±);Gcamp6f<sup>Lox/Lox</sup> or *Pdgfra*<sup>CreERT(±);Gcamp5-tdTomato<sup>Lox/Lox</sup>, Supplementary Fig. 1). We further validated its use on Ca<sup>2+</sup> imaging datasets from OPCs, OLs and myelin sheaths in control conditions and in different species and imaging setups from different laboratories working on Ca<sup>2+</sup> signals of these cells (see below).</sup></sup>

**Bleaching and noise correction.** The data input to Occam is a Ca<sup>2+</sup> imaging stack of frames recorded by microscopy acquisition software (see Supplementary Videos 1–3 as different examples). Occam performs specific processing steps for image stacks originating from different Ca<sup>2+</sup> imaging conditions. These processing steps are

summarized in Fig. 1a and in Supplementary manual. In the case of ex vivo wide-field Ca<sup>2+</sup> imaging stacks, Occam first performs a bleaching-correction step because this imaging condition often produces significant photobleaching (Fig. 1a; Supplementary Video 1). Such correction is not needed for imaging stacks originating in two-photon or miniscope experiments (Fig. 1a; Supplementary Video 2 and 3).

To correct for photobleaching, Occam fits the mean fluorescence intensity over time with a double exponential decay curve as follows:

$$y = A + B * \exp(-C * t) + D * \exp(-E * t)$$

where *A* is the offset of the intensity, *B* and *D* are the amplitude of each exponential and *C* and *E* are the characteristic time decay values of the *t* exponential. In this procedure, we encountered a difficulty in fitting the fluorescence decay due to large fluctuations in the mean intensity resulting from the high spontaneous Ca<sup>2+</sup> activity in oligodendroglia. To overcome this problem, we adapted the fitting procedure by generating several possible fits of the trace after removing sections with variable size and position. At the end of this step, a series of graphs are displayed showing the mean fluorescence intensity over time, the fit, the corrected mean fluorescence intensity of the image stack to which the fit applies, and the goodness of the fit (Supplementary manual). The user can then select the best fit for bleaching-correction step. If no single fit gives a reliable correction, the user can decide to skip this bleaching-correction step. Finally, the ratio between the raw and the fitted mean fluorescence intensity is calculated to obtain the corrected mean fluorescence intensity over time.

The software then performs noise corrections. For this step, we empirically tested different filter combinations allowing to both reduce the noise and increase the contrast. Wide-field image stacks from acute brain slices were the noisiest and required a combination of a Fourier transform filter, a rolling ball background subtraction and a Gaussian blur. Since the signal-to-noise ratio is better in image stacks from two-photon and miniscope images, their quality was not highly improved by this procedure, but we kept this correction to process all of the images for the next steps of segmentation in a similar fashion. In the miniscope experimental setting, the software configuration did not involve any use of the Fourier transform filter, which accelerates the data processing.

The noise-corrected image stack is then used to generate one image (called projection image) that will be used for the segmentation step (Fig. 1a). To define the most suitable projection image to perform the segmentation, we first tested several simple projection images, such as the standard deviation intensity projection. We found that



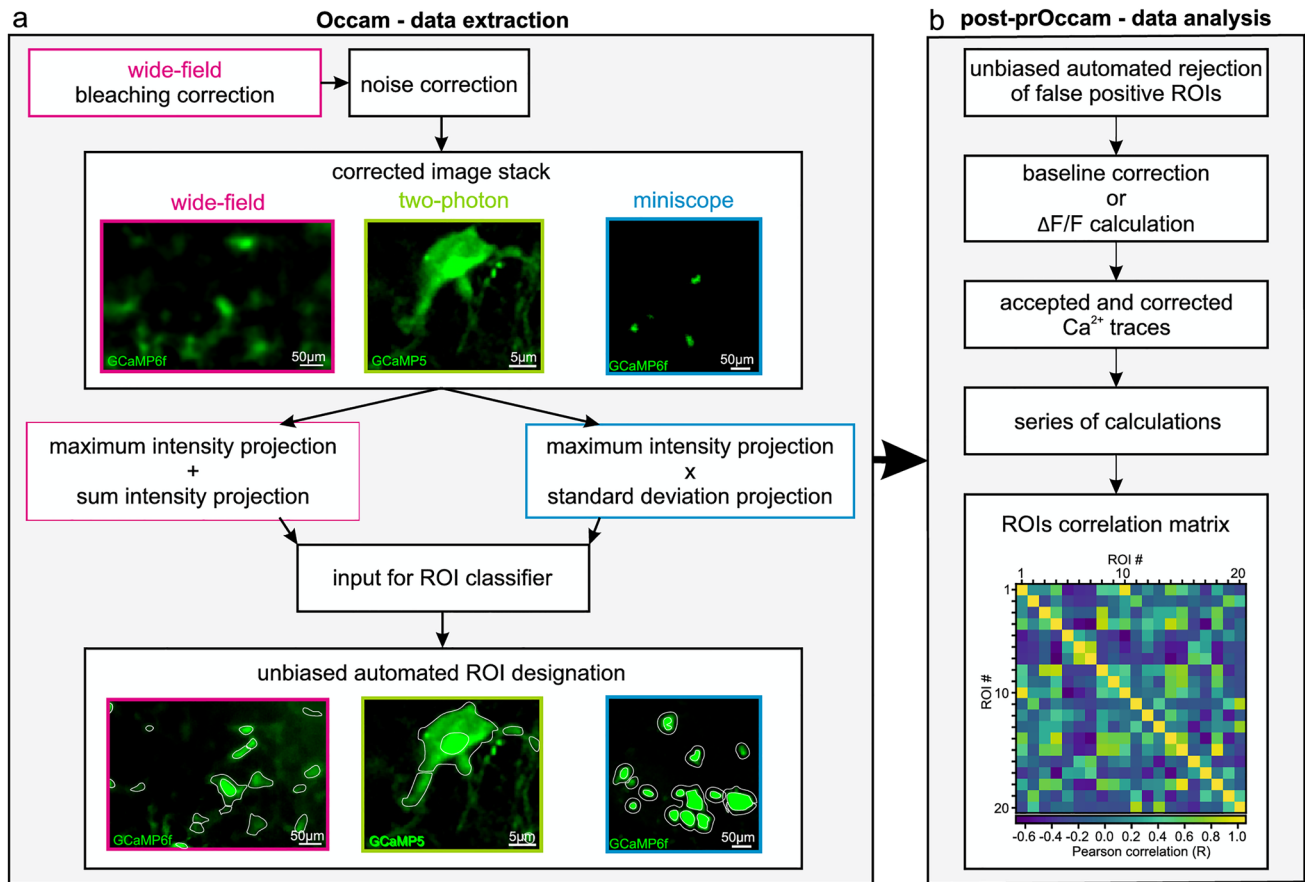


**Fig. 1** Occam and post-prOccam: an automated analysis software solution for oligodendroglia  $\text{Ca}^{2+}$  imaging of different preparations. **a** The Occam software is available as a Fiji/ImageJ2 plugin and configurable for the analysis of wide-field, two-photon and miniscope  $\text{Ca}^{2+}$  imaging. Occam performs bleaching correction only on wide-field image stacks and does noise correction according to the imaging condition (Supplementary manual). Then, it uses the maximum and sum intensity projections for wide-field and two-photon image stacks and the maximum and standard deviation projections for miniscope image stacks to build a projection image used as input for the WEKA-

based ROI classifier. **b** Output from Occam is fed to the post-prOccam Python-based software that (1) rejects any ROI that does not show significant  $\text{Ca}^{2+}$  fluctuations; (2) performs either baseline subtraction or the conventional  $\Delta F/F$  correction; (3) performs statistical calculations for each accepted ROI; and (4) computes a ROIs Pearson correlation matrix. Occam and post-prOccam are multiplatform, free and open source programs, freely available at: <https://gitlab.com/d5674/occam> (detailed procedures and software inner workings are described in the Supplementary manual)

simple projections were insufficient to detect all fluorescence fluctuations, which prompted us to test the combination of several types of projections into one single final projection image to improve the contrast. Through trial and error, we found that the best projection image in the case of wide-field and two-photon imaging stacks was obtained by summing the maximum intensity projection and the sum intensity projection. For miniscope image stacks, instead, the best projection image was produced by multiplying the maximum intensity projection with the standard deviation projection (Fig. 1a). The data processing performed by Occam to generate the final projection image thus depends on the  $\text{Ca}^{2+}$  imaging configuration mode set by the user upon starting of the processing (wide-field, two-photon and miniscope).

**Designation of active ROIs.** Occam performs the automatic ROI designation by harnessing the machine learning-based WEKA Fiji/ImageJ2 plugin that performs a trainable segmentation of frames [3] combined with a local maxima segmentation tool (Figs. 1a, 2a). First, WEKA is manually trained with the Occam-generated projection image to produce ROI classifiers for the three distinct imaging conditions, namely wide-field, two-photon, and miniscope. This training only takes a few minutes and is performed once with 3–5 projection images obtained from a subset of the image stacks originating in a given experiment setting. A minimum of two training classes are required to train WEKA and to produce a pixel-based segmentation (see below). We found, however, that four classes do better maximize the detection of regions with fluorescence intensity fluctuations (see [3])

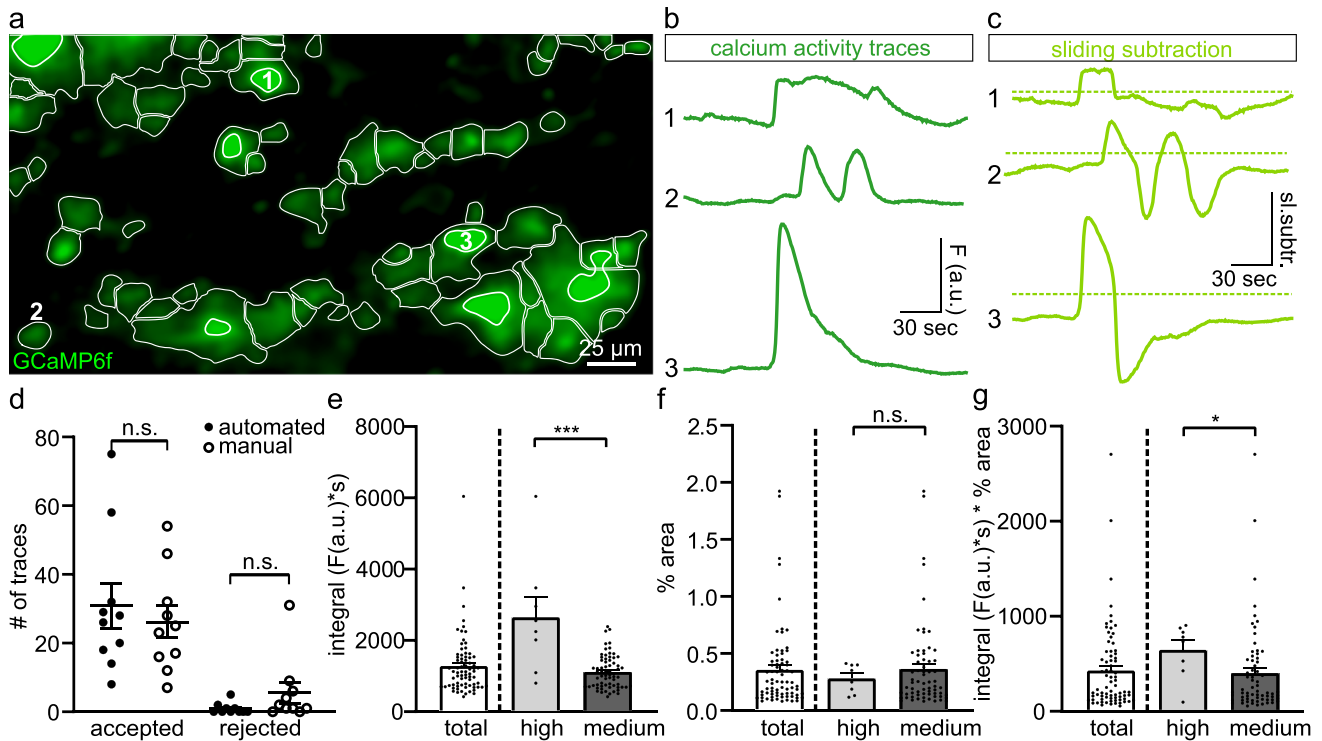


**Fig. 2** Analysis of wide-field  $\text{Ca}^{2+}$  signals of oligodendroglia in brain slices of LPC-induced demyelinated lesions [22]. **a** Representative projection image output by Occam with designated active ROIs (white) obtained from a  $40\times$  wide-field fluorescence imaging stack with GCaMP6f-expressing oligodendroglia in mouse callosal LPC-induced lesion. **b** and **c** Representative corrected ROI traces (**b**) and sliding window subtraction traces (**c**) as obtained with post-prOccam. **d** Comparison of the manual rejection of false-positive ROIs and the automatic rejection of false-positive ROIs by post-prOccam revealed

no differences in accepted and rejected ROIs, validating post-prOccam's performance. *n.s.*: not significant, two-way ANOVA followed by a Bonferroni multiple comparisons test. **e–g** Calculations performed by post-prOccam on each individual ROI of the image stack include the integral (**e**), the percentage of active area (**f**) and the integral multiplied by the percentage of active area (**g**). The calculations are performed separately for high and medium intensity ROIs.  $*p < 0.05$  and  $***p < 0.001$ ; Mann–Whitney test

for details of WEKA plugin). We named these classes (1) high, (2) medium, (3) low and (4) background matching their relative mean pixel intensities. High and medium classes define regions with very high and intermediate pixel intensities, respectively, and, therefore, represent those that most likely detect true fluorescence changes. These regions are considered as active ROIs during data analysis while low and background mean pixel intensity ROIs (dark and very dark, respectively) are considered as background and are discarded. During data processing, the ROI classifier and WEKA are called by Occam to obtain a first segmentation. However, because WEKA needs training by the user, its operation while performing the segmentation might suffer from some bias. To overcome this potential problem, Occam combines the results obtained by WEKA with those obtained by an automatic and unsupervised segmentation based on local maxima. Of note, this procedure was designed to detect ROIs showing fluorescence fluctuations and not ROIs having constant fluorescence values because the projection image used for the segmentation mainly reveals fluorescence changes. At the end of the segmentation procedure, Occam

designates a ROI as a vector of mean fluorescence intensity values of the corresponding region in the different frames of the stack (that is, over the acquisition time points). Such ROI vectors are also indifferently called ROI traces or ROIs in this report.

Datasets obtained by in vivo imaging proved particularly challenging because the large number of frames in the stacks (as a result of long acquisition times) yielded a useless projection image, because  $\text{Ca}^{2+}$  signals might have occurred either as a too short event or as a too intense and prolonging event. To enhance the precision of ROI detection by Occam in such large data files, the program first splits the image stack into a configurable number of sub-stacks that are in turn processed as described above to yield a projection image for each sub-stack (Fig. 3a). Another challenge that we encountered is that this procedure can lead to an overestimation in the number of active ROIs if a specific region of the stack is active several times during a single experiment and is thus detected as a different ROI in multiple sub-stacks. In this specific situation, the user can configure a setting value defining the ROI overlapping tolerance level

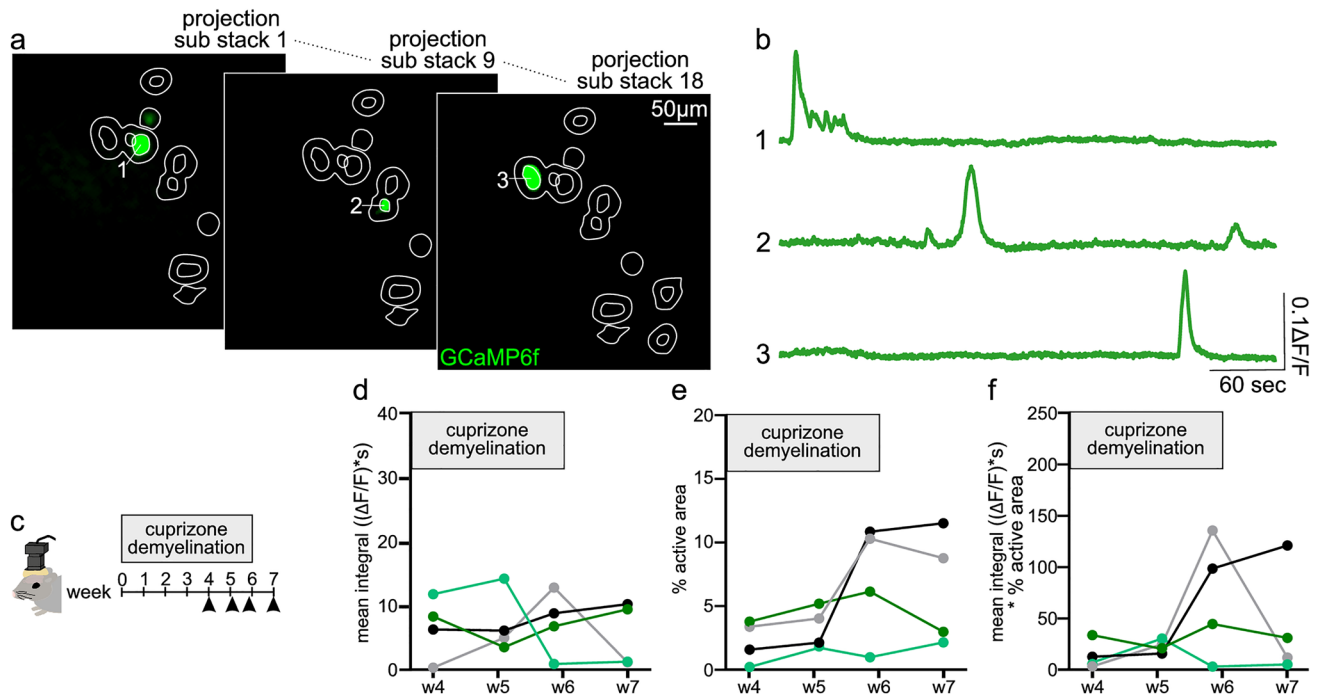


**Fig. 3** Analysis of miniscope  $\text{Ca}^{2+}$  signals of oligodendroglia in freely moving mice. **a** Representative images of an in vivo microendoscopy  $\text{Ca}^{2+}$  imaging stack collected from a demyelinated corpus callosum of a freely moving mouse. The image displays detected active ROIs (white) in several sub-stacks as obtained with the in vivo analysis option of Occam and **b** their corresponding corrected  $\text{Ca}^{2+}$  traces obtained with post-prOccam. **c** Longitudinal experiments that

can be analyzed with Occam and post-prOccam over weeks. Four mice were fed with the cuprizone diet to induce demyelination (see Supplementary Material and Methods) and  $\text{Ca}^{2+}$  imaging was performed for four consecutive weeks. **d** Mean integral, **e** % of active area and **f** mean integral multiplied by percentage of active area are calculated with post-prOccam over the four consecutive weeks for all mice

above which overlapping ROIs are merged into a single ROI (Fig. 3a; Supplementary manual). The described procedure segments large image stacks from either a single acquisition or from multiple acquisitions performed on the same animal over weeks (Fig. 3a–f).

From a user experience stand point, Occam features a graphical user interface that allows the user to easily and intuitively configure various aspects of the data processing. In particular, the user selects one configuration predetermined for the analysis of oligodendroglia  $\text{Ca}^{2+}$  imaging stacks from one of the three supported imaging conditions, namely (i) wide-field, (ii) two-photon, and (iii) miniscope imaging stacks, (Fig. 1a; Supplementary Videos 1–3). The Occam program can, therefore, be used for automated and customizable detection of active ROIs in  $\text{Ca}^{2+}$  imaging stacks and even allows for precise segmentation in large stacks obtained during long recordings. In addition, Occam makes the preprocessing of longitudinal in vivo  $\text{Ca}^{2+}$  imaging experiments feasible with quick image segmentations for data obtained over multiple days or weeks.

To further confirm that Occam successfully performs ROI designation, we tested the program on two simulated datasets which allow us to independently examine

two different situations: (1) transient objects with different sizes and shapes, and (2) different objects changing location (freely available at <https://github.com/yu-lab-vt/Aqua> [30]). The first situation was analyzed using the two-photon configuration which allows for the visualization of isolated events, while the second one was analyzed using the miniscope configuration which captures brief overlapping events. In the two different conditions, Occam's ROIs fit the shape of almost all events (Supplementary Fig. 2). Using five consecutive images of the stack to quantify the number of detected ROIs, we found that Occam detected 38 out of 37 objects in the first case (Supplementary Fig. 2a) and 26 out of 28 objects in the second case (Supplementary Fig. 2b, c), confirming that it is capable of detecting most of the events in simple and complex situations.

Upon processing of any given image stack of frames, Occam produces a corresponding set of tabular data files that contain descriptions of the mean fluorescence intensity of each ROI along the time-resolved acquisition experiment. These files are then fed to the post-prOccam software for ROI refinement and statistical calculations (Fig. 1b).

## Post-prOccam performs automated ROI refinement, quantifications and correlations

The post-prOccam software processes the files produced by Occam according to user-defined settings determining the ROI processing and filtering stringency, as defined in a configuration file (Supplementary Files 1–3).

**Rejection of false-positive ROIs.** First, post-prOccam was designed to reject false-positive ROIs (Fig. 1b). Automated ROI detection algorithms cannot be error-free and almost always require post-processing aimed at rejecting false-positive ROIs [8]. To reject false-positive ROIs, we adapted an algorithm previously used for the fluorescence-based tracking of exocytotic events [33], Supplementary manual). Based on repeated intensity value subtractions in a sliding window over the whole ROI vector of mean fluorescence intensity values (Supplementary Fig. 3a–c), our method allowed us to detect fluorescence intensity changes that were greater than noise fluctuations. For this, we had to take into account the long-lasting kinetics of  $\text{Ca}^{2+}$  signals from OPCs and OLs in the three tested imaging conditions (Supplementary Fig. 4). In the case of wide-field image stacks, for instance, the sliding window subtractions were computed between points distanced by 40 frames, a value close to the measured rise time of several  $\text{Ca}^{2+}$  events (Fig. 2b, c; Supplementary Fig. 4a; rise time:  $54.63 \pm 9.67$  frames equivalent to  $35.25 \pm 5.36$  s,  $n=34$  events from  $n=8$  fields). The sliding window subtraction is performed according to the following calculation:  $\text{ROI}[n] = \text{ROI}[n+40] - (\text{ROI}[n])$ , with  $n$  being the frame number in the stack ( $n$  is incremented by 1 after each such calculation; Supplementary Fig. 3a–c). Each initial ROI trace is thus replaced by a new one, as computed from the sliding window subtractions, that is then tested against user-defined threshold parameters set in the configuration file (Supplementary Files 1). These threshold settings configure the rejection of ROI traces depending on both their  $\text{Ca}^{2+}$  event kinetics and noise. To find the best settings to eliminate false-positive traces, we empirically tuned the threshold parameters and compared the results with those obtained by manually rejecting ROIs in several imaging stacks (Fig. 2d). The threshold values that were found to be the most effective in rejecting false-positive ROIs were a sliding subtraction window of 40 points and a mean absolute deviation factor of 1.5 based on  $\text{Ca}^{2+}$  signal characteristics and the noise fluctuations, and were set as default values in the configuration file provided in Supplementary File 1 (Fig. 2a–c; see the detailed description of the threshold parameters in the Supplementary manual). A similar procedure was applied for determining the most suitable parameters to analyze two-photon and miniscope image stacks (Supplementary File 2–3).

**ROI trace correction.** ROIs that are accepted by post-prOccam for further analysis are then corrected either by

performing a baseline subtraction or by calculating  $\Delta F/F$ , as defined by the user in the configuration file (Fig. 1b; Supplementary manual and Files 1–3). In the case of baseline subtraction, the mean minimum intensity value calculated from a configurable number of trace points around the minimum intensity value of the ROI is subtracted from the ROI trace whereas, in the case of  $\Delta F/F$  trace correction, the  $\Delta F/F = [(F(t) - F_0)/F_0]$  computation is performed on the ROI trace ( $F_0$  is the mean minimum intensity value). We implemented these two options because in the case of wide-field microscopy, we found that a baseline subtraction computation was better adapted than the conventional  $\Delta F/F$  to the analysis of the oligodendroglia  $\text{Ca}^{2+}$  signal dynamics. Indeed, the oligodendroglial cells in acute brain slices exhibited overall high levels of background noise and high levels of spontaneous  $\text{Ca}^{2+}$  activity, often right at the start of the recording, making it difficult to determine with certainty the real  $F_0$  resting fluorescence intensity value (Fig. 2a–b, Supplementary Fig. 4a, d–e). For two-photon and miniscope imaging stacks, determination of the resting fluorescence was feasible and, therefore, we used the  $\Delta F/F$  ROI trace correction option (Fig. 3b; Fig. 6a, e).

**Statistical calculations on corrected ROI traces.** The accepted and corrected ROI traces are output to a file for further statistical processing, such as, for example, the calculation of the surface area of each ROI in pixels, the ROI integral, the sum of all the ROIs integrals and of all the ROIs surface areas in pixels. The results of these calculations are output to a file (Fig. 1b; Supplementary manual). Figure 2e–g illustrates calculation results obtained on each ROI in a single image stack; Fig. 3d–f shows the calculation results for all the ROIs in several image stacks from four mice recorded during several weeks. Since the complex features of oligodendroglial  $\text{Ca}^{2+}$  events make it difficult their proper individual isolation (Supplementary Fig. 4), we found it more appropriate to calculate the mean intensity integral of each ROI trace rather than to use a procedure for single event detection [4], see Discussion). When using single event detection procedures, complex events are oversimplified even though they are characteristic of both OPCs and OLs and should, therefore, be taken into account (Fig. 6, Supplementary Fig. 4). Using the mean intensity integral of the ROI trace implies that all  $\text{Ca}^{2+}$  events in their entirety are considered in the analysis. As expected, high intensity ROIs exhibited significantly larger mean integrals than medium intensity ROIs (Fig. 2e) and, despite similar mean percentage of active area between high and medium intensity ROIs (Fig. 2f), the mean integral multiplied by the percentage of the active area remained larger for high intensity ROIs (Fig. 2g). However, when considering all the analyzed stacks, the number of high intensity ROIs was always considerably smaller than the number of medium intensity ROIs (high intensity ROIs:  $n=3.5 \pm 0.9$ ; medium intensity



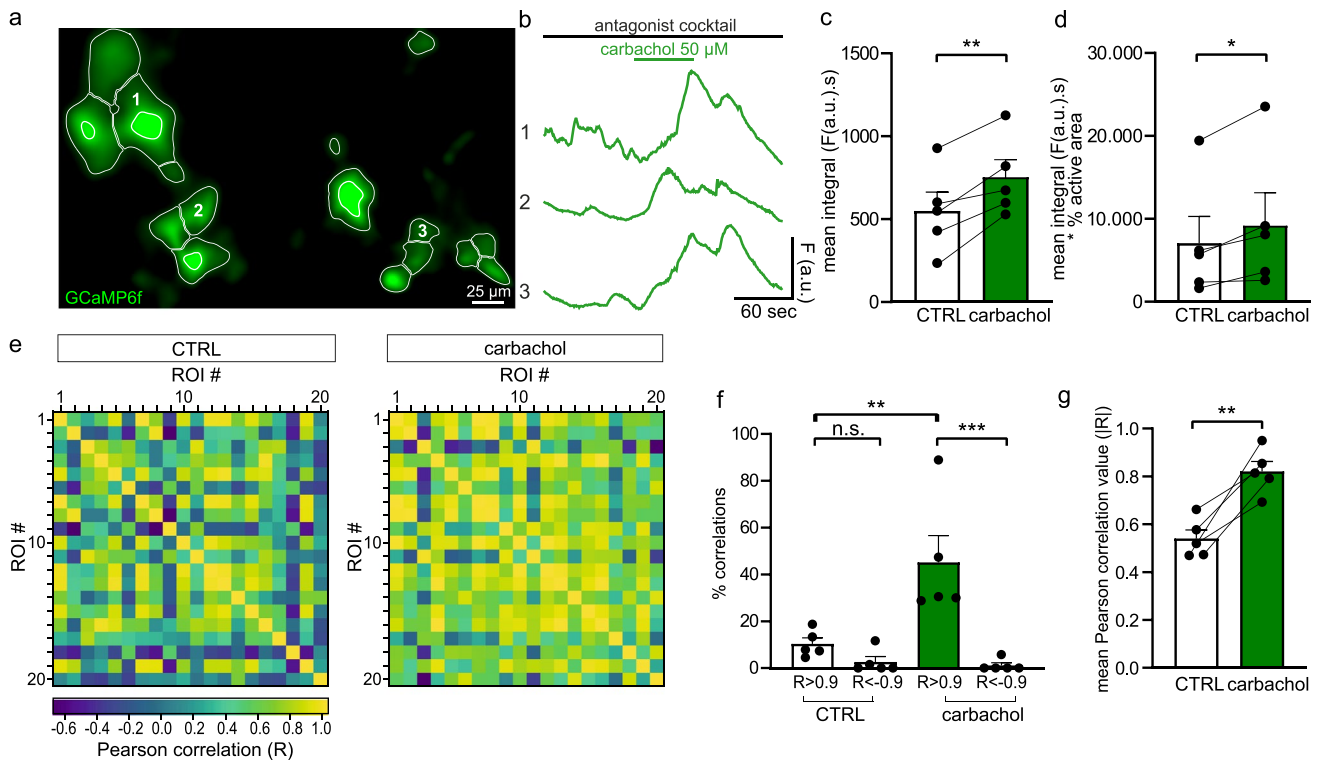


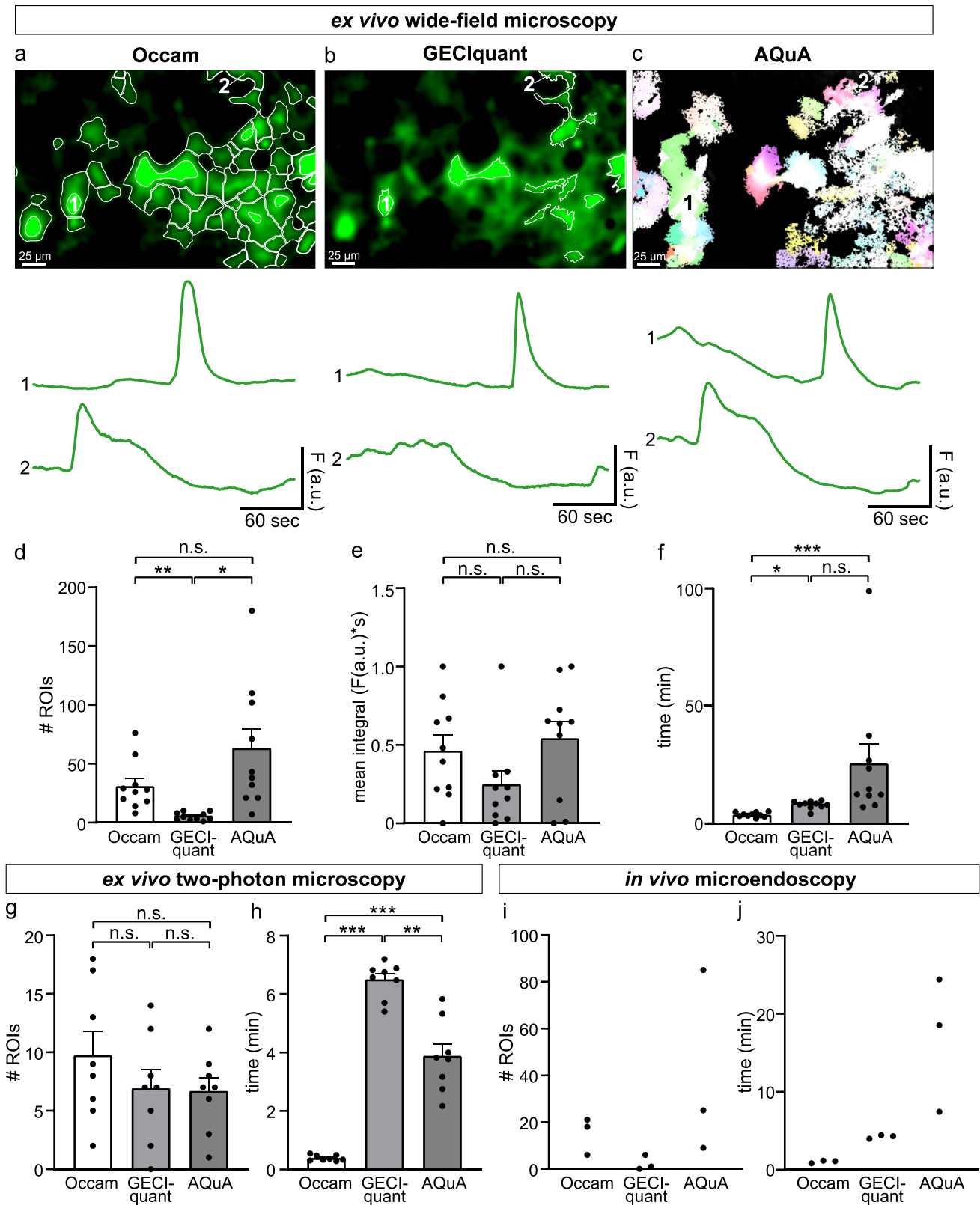
**Fig. 4** ROI interval-based analysis and evaluation of  $\text{Ca}^{2+}$  signal synchronization in oligodendroglia. **a** Representative image of  $\text{Ca}^{2+}$  imaging in callosal LPC-induced lesions in ex vivo brain slices that were exposed to  $50 \mu\text{M}$  carbachol to induce increases in  $\text{Ca}^{2+}$  signals in oligodendroglia in the presence of an antagonist cocktail containing  $10 \mu\text{M}$  NBQX,  $50 \mu\text{M}$  AP5,  $10 \mu\text{M}$  GABAazine,  $1 \mu\text{M}$  TTX and  $50 \mu\text{M}$  mecamylamine. The image displays detected active ROIs (white) as obtained with Occam. **b** Representative corrected  $\text{Ca}^{2+}$  traces obtained with post-prOccam from callosal LPC-induced demyelinated lesions in brain slices that were exposed to  $50 \mu\text{M}$  carbachol to induce an increase in  $\text{Ca}^{2+}$  signals in oligodendroglia in the presence of a cocktail of antagonists containing  $10 \mu\text{M}$  NBQX,  $50 \mu\text{M}$  AP5,  $10 \mu\text{M}$  GABAazine,  $1 \mu\text{M}$  TTX and  $50 \mu\text{M}$  mecamylamine. **c** and **d** Mean integral (**c**) and mean integral multiplied by the percentage of active area (**d**) of  $\text{Ca}^{2+}$  signals in control and after exposure to carbachol.  $*p < 0.05$ ,  $**p < 0.01$ ; paired Student's *t*-test. **e** Example of correlation matrices obtained with post-prOccam before and after

carbachol exposure. Each square indicates the Pearson correlation value of one ROI with another. Yellow indicates high positive Pearson correlation, while dark blue indicates high negative correlations. Note that traces 1, 2, 3 in panel a correspond to ROIs 7, 12, 14 in the matrix. **f** The percentage of correlations in the correlation matrix that is significantly negative ( $R < -0.9$ ) or significantly positive ( $R > 0.9$ ) in both control and carbachol exposed conditions. *n.s.*: not significant,  $**p < 0.01$ ,  $***p < 0.001$ , two-way ANOVA followed by a Tukey's multiple comparisons test. **g** Mean Pearson correlation values for control and carbachol conditions. CTRL: control before carbachol exposure ( $n = 5$  stacks,  $n = 5$  slices,  $n = 4$  mice). Note that post-prOccam successfully identified the expected enhanced synchronization of  $\text{Ca}^{2+}$  signals upon carbachol application, validating its correlation analysis capabilities.  $**p < 0.01$ ; paired Student's *t*-test. CTRL: control before carbachol exposure ( $n = 5$  stacks,  $n = 5$  slices,  $n = 4$  mice). Dot plots are presented as mean  $\pm$  s.e.m

ROIs:  $n = 27.3 \pm 5.7$ ; total ROIs:  $n = 30.8 \pm 6.5$  for  $n = 10$  stacks,  $N = 7$  mice). Moreover, the mean integral of medium intensity ROIs and that of all pooled data (Total) remain similar (Fig. 2e). Therefore, the data from high and medium intensity ROIs are pooled by post-prOccam for subsequent quantifications; however, we kept their Occam-based detection separate because the WEKA plugin performed better when classifying ROIs in these two categories.

**ROI interval-based analysis.** One important feature of post-prOccam is its ability to compare ROIs only at specific acquisition time point intervals of the recorded datasets. For instance, in the case of applications of pharmacological agents during  $\text{Ca}^{2+}$  imaging recordings, a user might wish to

compare  $\text{Ca}^{2+}$  signals in the absence or in the presence of a drug in a single image stack. The default post-prOccam software behavior is to perform all the calculations described in the previous sections on the whole ROI vector (that is, for all the acquisition time points). However, in the specific cases mentioned above, it might be useful for the calculations to be performed only over selected ranges of the ROI vector (that is, intervals of that ROI's acquisition time points). The configuration file provides a section in which the user might list any number of ROI vector intervals over which to perform the previously described calculations (Supplementary Files 1–3). To validate this feature, we bath-applied the muscarinic receptor agonist carbachol in the presence



of a cocktail of antagonists to stimulate intracellular  $Ca^{2+}$  signals of oligodendroglia during wide-field  $Ca^{2+}$  imaging recordings (Fig. 4a, b). Oligodendroglia express muscarinic

receptors M1, M3 and M4, which, when activated by carbachol, increase intracellular  $Ca^{2+}$  signals [1, 10, 31]. Our tests showed that post-prOccam can indeed detect the expected

◀ **Fig. 5** Comparison of Occam, GEClquant and AQuA for the analysis of wide-field, two-photon and miniscope oligodendroglial  $\text{Ca}^{2+}$  imaging data. Representative ROI detection and  $\text{Ca}^{2+}$  traces obtained by analysis with Occam (a), GEClquant (b) and AQuA (c). ROI number (d), normalized mean integrals (e) and time of analysis per stack (f) obtained with Occam, GEClquant and AQuA in wide-field imaging. ROI number (g) and time of analysis per stack (h) for two-photon imaging and ROI number (i) and time of analysis (j) for miniscope obtained with Occam, GEClquant and AQuA. No statistical test was applied for miniscope data since the  $n$  size was small. n.s.: not significant. \* $p < 0.05$ , \*\* $p < 0.01$ , \*\*\* $p < 0.001$  one-way ANOVA test followed by a Tukey's multiple comparison test or the non-parametric Friedman test followed by a Dunn's multiple comparison test. Dot plots are presented as mean  $\pm$  s.e.m

increase in intracellular  $\text{Ca}^{2+}$  signals in oligodendroglia upon bath application of 50  $\mu\text{M}$  carbachol in the presence of a cocktail of antagonists, as revealed by an increase in the mean integral compared to control conditions (before carbachol application; Fig. 4a–d).

*Analysis of synchronized  $\text{Ca}^{2+}$  signals.* While it is now established that a population of astrocytes may exhibit high levels of  $\text{Ca}^{2+}$  activity synchronization in vitro and in vivo [13, 15], nothing is known about the potential of  $\text{Ca}^{2+}$  signals in oligodendroglia to be synchronized. We thus implemented in post-prOccam a correlation calculation which allows the user to establish whether ROIs within a given image stack show synchronized  $\text{Ca}^{2+}$  signals. The post-prOccam program computes an inter-ROI Pearson correlation coefficient matrix between each ROI trace and every other ROI trace (Fig. 4e; see “Materials and methods”; [13]. In control conditions (before carbachol application), we found that most ROIs did not show any correlated  $\text{Ca}^{2+}$  activity, as evidenced by a low percentage of correlated ROIs ( $|R| < 0.9$ ) and a mean Pearson correlation coefficient  $R$  value of  $0.54 \pm 0.24$  (Fig. 4e–g). As expected for a carbachol application experiment, which forces the simultaneous activation of oligodendroglia (Fig. 4a), we observed a significant overall increase of the positive inter-ROI  $\text{Ca}^{2+}$  activity correlation level (Fig. 4e–g), with a mean Pearson correlation value of  $0.82 \pm 0.04$  in the presence of carbachol. These results confirmed that the post-prOccam software successfully determined the level of  $\text{Ca}^{2+}$  activity correlation between ROIs and was able to detect simultaneous increases of that activity as induced by pharmacological agents. In order to adapt to any specifics of biological applications, the Pearson correlation  $R$  value threshold might be configured. The percentage of correlated ROIs as well as the mean Pearson correlation coefficient are reported for each image stack in the corresponding output file generated by the post-prOccam.

Finally, for informational and debugging purposes, a log file is produced by post-prOccam with a highly detailed account of all the data processing steps and their outcome. The accepted ROIs and the corresponding processed data of

a stack are saved by post-prOccam in two separate files for further statistical analysis. Of note is our helper pp-supervisor program that allows the scientist to run post-prOccam automatically over a set of stack data directories, all located in a single master directory. The program either picks the configuration file located in each stack data directory or can be instructed to use the same configuration file located elsewhere. Taken together, the Occam and the post-prOccam software programs provide a configurable and automatable solution for the analysis of oligodendroglial  $\text{Ca}^{2+}$  signals.

### Comparison of the capabilities of our package with those of other programs

Occam was compared to two other available programs, GEClquant and AQuA [29, 30] using three different imaging datasets wide-field, two-photon, and miniscope. Both GEClquant and AQuA are Fiji/ImageJ2 plugins that have recently been employed for the analysis of  $\text{Ca}^{2+}$  signals in oligodendroglia [17, 18]. To perform an unbiased comparison, we kept the same parameters of spatial and temporal resolution and minimum pixel size of ROIs, and we optimally tuned the other parameters for each method. Figure 5a–c illustrates the ROIs detected by the three programs in a wide-field oligodendroglia  $\text{Ca}^{2+}$  imaging stack. Of note, because event detection by AQuA does not use a ROI-based approach, we considered the trajectory of events as ROIs for the comparison (Fig. 5c). We found no significant difference between either the number of ROIs or their localization in the image as detected by AQuA and Occam (Fig. 5a, c, d; % of area occupied by AQuA ( $30.8 \pm 1.6\%$ ) and Occam ( $40.9 \pm 1.2\%$ ), Paired  $t$  test,  $p = 0.116$ ). We noted that AQuA tended to recognize more ROIs than Occam in some stacks and, conversely, GEClquant detected a significantly smaller number of ROIs as compared to both Occam and AQuA (Fig. 5a–d). The normalized mean integral of all detected ROIs was not significantly different between the three programs, which was expected since this value is independent of the number of ROIs (Fig. 5e). However, an interesting observation is that the three tested programs did perform differently in terms of photobleaching correction, with Occam performing a better photobleaching correction than both GEClquant and AQuA, as assessed by manual inspection of the results (Fig. 5a–c, traces). A proper photobleaching correction is desirable when performing analyses on  $\text{Ca}^{2+}$  imaging datasets obtained in experiments in which drugs are applied because the photobleaching might mask the appearance of the drug effects. Similar results were obtained in in vivo microendoscopy datasets where the number of ROIs detected by GEClquant was very low as compared to Occam and AQuA (Fig. 5i). Moreover, manual scrutiny of AQuA results showed that it overestimated the number of events detected in one miniscope  $\text{Ca}^{2+}$  imaging stack where events are detected in regions of the field showing weak regular

fluctuations in background illumination, but do not correspond to  $\text{Ca}^{2+}$  transients (Fig. 5i), but it was not possible to find better parameters to optimize the detection. While Occam appears to perform a more faithful ROI detection and photobleaching correction on wide-field imaging stacks from both wide-field and miniscope  $\text{Ca}^{2+}$  imaging, all three programs detected similar number of ROIs in two-photon imaging stacks (Fig. 5g). Overall, Occam is distinctly more flexible in the analysis of widely differing image stacks originating from different imaging conditions. This observation is consistent with the fact that GECIquant and AQUa were designed and have mainly been used for two-photon  $\text{Ca}^{2+}$  imaging. From an operational point of view, Occam required significantly less manual input from the user and was more than four times faster (up to 30 times faster) than the other two programs (Fig. 5f, h, j). Occam's speed is an advantage when analyzing a large number of stacks as it makes the analysis more systematic. Compared to AQUa, not only does Occam use less random-access memory (RAM), but it also occupied much less disk space. For comparison, Occam's analysis of three miniscope  $\text{Ca}^{2+}$  imaging stacks used 1 GB compared to 30 GB for AQUa (0.53 GB for GECIquant). This makes the analysis with Occam easily feasible on any personal computer and more suitable for miniscope data which often relies on large image stacks and data acquired over multiple imaging sessions.

### Occam and post-prOccam analyze $\text{Ca}^{2+}$ signals from OPCs, OLs and myelin sheaths in diverse species and imaging conditions

We sought to validate whether Occam and post-prOccam could successfully analyze  $\text{Ca}^{2+}$  signals from different cells of the OL lineage, in different species and preparations. Therefore, we used our software to analyze the  $\text{Ca}^{2+}$  activity of OPCs, OLs and myelin sheaths from our own data as well as data obtained in other laboratories. Our software did analyze independent  $\text{Ca}^{2+}$  signals both in the soma and fine processes of OPCs from mouse corpus callosum slices following demyelination (Fig. 6a; our own data) and from in vivo mouse somatosensory cortex in control (Fig. 6b; [11]). Notably, when analyzing a wider field of view in the in vivo mouse visual cortex (Fig. 6c, [18]) or in the in vivo zebrafish spinal cord (Fig. 6d; Bispo and Czopka, unpublished data), our software detected  $\text{Ca}^{2+}$  activity in fine OPC processes not visibly connected to a soma. Occam and post-prOccam analyzed only active areas of the OPCs, excluding inactive areas of the OPCs that nevertheless exhibited a constant fluorescence. The programs also performed well when analyzing  $\text{Ca}^{2+}$  activity in image stacks obtained in the soma and processes of OLs recorded in mouse demyelinated lesions in acute slices (Fig. 6e; our own data) and in primary mouse cell cultures (Fig. 6f; [14]). Finally, it performs equally well in detecting ROIs in myelin sheaths recorded

in vivo in the zebrafish spinal cord (Fig. 6g, Braaker and Lyons, unpublished data) and the mouse somatosensory cortex (Fig. 6h; Supplementary Video 1 from [6]). To test the performance of our software, we further compared the number of active ROIs that could be distinguished by visual inspection in single cells with that of the active ROIs automatically detected. We found that the automated analysis yields significantly more active ROIs (Fig. 6i).

Taken together, these results show that Occam and post-prOccam detect  $\text{Ca}^{2+}$  events in soma and processes of OPCs, OLs and in myelin sheaths from diverse preparations in healthy and pathological conditions. In addition, Occam and post-prOccam analyzed various  $\text{Ca}^{2+}$  indicators, including cytosolic (Fig. 6a, b, e, f, h) and membrane-bound  $\text{Ca}^{2+}$  indicators (Fig. 6c, d, g).

## Discussion

While it is suspected that oligodendroglial  $\text{Ca}^{2+}$  activity plays a key role in myelination and myelin repair, the characteristics of oligodendroglial  $\text{Ca}^{2+}$  signals remain largely unexplored. This is due to a limited number of ex vivo and in vivo  $\text{Ca}^{2+}$  imaging studies as well as a lack of automated imaging data analysis programs adapted to the monitoring of the specific characteristics of oligodendroglial  $\text{Ca}^{2+}$  signals. To fill this need, we developed a software package comprising two programs, Occam and post-prOccam, that implement an analytical workflow for the automated in-depth analysis of one- and two-photon oligodendroglial  $\text{Ca}^{2+}$  imaging data. Tested in MS Windows (version 10) and Debian GNU/Linux (versions 10 and 11), this cross-platform software was designed to be easily configurable to ensure an unbiased selection of active ROIs and to allow the analysis of large datasets. Licensed under the GNU GPLv3 + Free Software license, both programs can be freely used, modified according to any specific need and question, and redistributed.

Since our software package has been developed for our specific needs in  $\text{Ca}^{2+}$  imaging data analysis of oligodendroglial cells, it performs optimally with this kind of data. It is worthwhile noting that, because the  $\text{Ca}^{2+}$  signal detection is finely configurable, our software may be suited to new use cases such as the study of other glial cell types. Occam's features for in vivo experiments have been adapted so that it could detect not only fast-occurring events, but also the repeated activation of a single region over a long experiment. Occam could successfully and quickly analyze long microendoscopy recordings taken repeatedly over a period of weeks on the same mouse. These results pave the way for future research on oligodendroglial  $\text{Ca}^{2+}$  signaling in the living mammalian brain during animal behavior studies and in different experimental conditions. Of note, potential motion artifacts may occur in the recordings due to movements of



the slice (ex vivo) in the recording chamber or the brain (in vivo) during behavior. Image distortions caused by motion can be dealt with, prior to  $\text{Ca}^{2+}$  analysis, using existing tools such as StackReg and Turboreg ImageJ plugins [28].

During post-prOccam data processing, false-positive ROIs with too small  $\text{Ca}^{2+}$  fluctuations are rejected, which can be construed as a refinement of the ROI detection process. We found that this automatic  $\text{Ca}^{2+}$  trace selection performs equally well as a manual  $\text{Ca}^{2+}$  trace selection. Among other analysis options, the ability to restrict the processing and quantification steps to specific acquisition intervals has

proven useful to screen the effect of drugs on oligodendroglial  $\text{Ca}^{2+}$  signaling. Furthermore, inter-ROI correlation calculations by post-prOccam help make it possible to spotting synchronized  $\text{Ca}^{2+}$  signals across different ROIs in a given image stack. We validated these analysis modalities by successfully detecting, quantifying and correlating  $\text{Ca}^{2+}$  activity increases upon carbachol bath application to ex vivo mouse brain slices. The implementation of a correlation analysis prompts future research into the synchronization and propagation of  $\text{Ca}^{2+}$  signals within and between OL lineage cells.

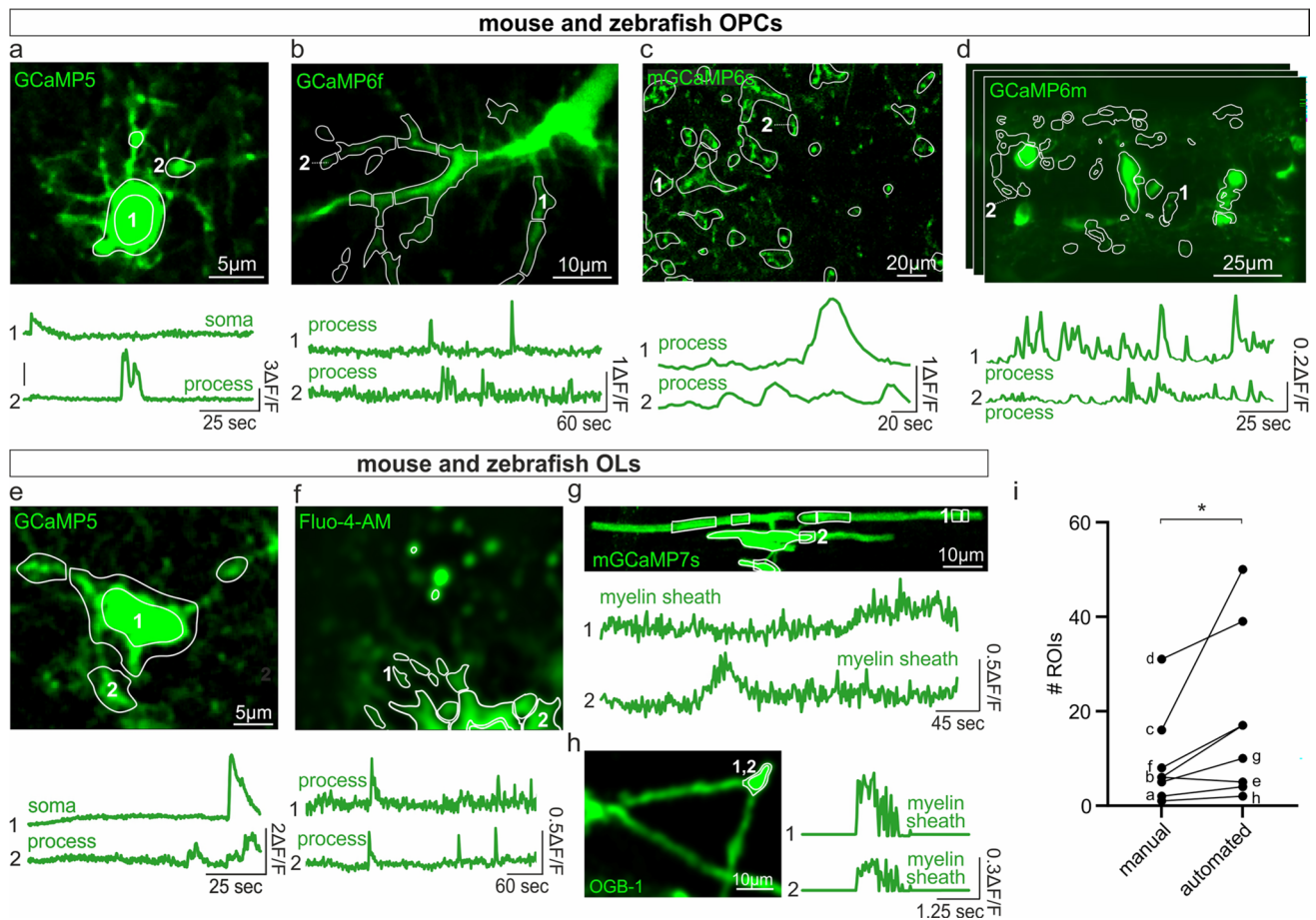


**Fig. 6** Occam and post-prOccam analyze  $\text{Ca}^{2+}$  signals from OPCs, OLs and myelin sheaths in different species and imaging conditions. Representative images with ROIs (white) and  $\text{Ca}^{2+}$  traces obtained with Occam and post-prOccam for (a) a putative OPC from mouse demyelinated corpus callosum in acute slices recorded in a two-photon microscope (see “Materials and methods”), (b) an OPC from the in vivo mouse somatosensory cortex recorded with a two-photon microscope (Supplementary Video 1 from [11]), (c) OPC processes from the in vivo mouse visual cortex recorded with a two-photon microscope (Supplementary Video 3 from [18]), (d) OPC somata and processes from the in vivo zebrafish spinal cord recorded with a light sheet microscope (from Tim Czopka & Patricia Bishop, Unpublished data), (e) a putative OL from mouse demyelinated corpus callosum in acute slices recorded with a two-photon microscope (see “Materi-

als and methods”), (f) a primary mouse OL in culture recorded with an Opterra II Multipoint Swept Field Confocal microscope (Supplementary Video 1 from [14]), (g) an OL process from the in vivo zebrafish spinal cord recorded with a Confocal Zeiss LSM880 Airyscan (from Philipp Braaker and David Lyons, unpublished data) and (h) an OL process recorded in an acute brain slice from a mouse with an Olympus BX61WI microscope and a NeuroCCD camera at 40 Hz (Supplementary Video 1 from [6]). The image stacks were recorded at different acquisition rates and analyzed with Occam using either two-photon (a, b, c, f, g) or miniscope configuration (d). **i** Comparison of the number of ROIs identified by visual inspection with that of ROIs automatically detected in the different analyzed stacks. \* $p < 0.05$ ; Wilcoxon rank test. Dot plots are presented as mean  $\pm$  s.e.m

Ca<sup>2+</sup> events of OPCs and OLs are unique in their variability and duration. Unlike neurons, which exhibit well-defined Ca<sup>2+</sup> signals on a millisecond scale [9], both OPCs and OLs show complex Ca<sup>2+</sup> events characterized by very slow and variable kinetics that make their detection and isolation difficult, particularly because of their frequent convolution (Supplementary Fig. 4). We, therefore, found that it was easier to quantify them using ROI-based measurable dimensions, such as the number of ROIs, size and mean pixel intensity integral, than using the frequency, amplitude and duration of isolated events. This complexity of oligodendroglia Ca<sup>2+</sup> events has previously been observed with two-photon microscopy [4] and in recordings at single-cell resolution [5, 6, 16, 19], indicating that complex Ca<sup>2+</sup> dynamics are a hallmark of OL lineage cells. Thresholding techniques or event template detection methods, commonly used on neuron and astrocyte Ca<sup>2+</sup> imaging datasets, are not easily applicable to the unique and complex Ca<sup>2+</sup> events observed in oligodendroglia. For this reason, we evaluate activity levels by measuring the number and size of active ROIs as well as the integral of the traces. Our measurements thus account for the activity throughout the whole ROI trace or during configurable intervals without isolating Ca<sup>2+</sup> activity events. However, integral values take more into account spatial than temporal features of Ca<sup>2+</sup> events, and the latter may be important for OL lineage cells under certain conditions [5]. In this case, the user could define successive intervals in the post-prOccam configuration file to analyze the evolution of the integral over time for a single stack. In the eventuality that a detailed description of Ca<sup>2+</sup> events would be desirable, extra measurements may be performed either manually or by other post-processing programs on the corrected active ROI traces as output by post-prOccam. Supplementary Fig. 5 illustrates the analysis of individual Ca<sup>2+</sup> events for our datasets acquired in the three different conditions, i.e., wide-field, two-photon and miniscope. Although the complexity of events is largely underestimated in these analyses, it is clear that the duration of Ca<sup>2+</sup> events lasted from a few seconds to minutes, independent of the imaging condition (see also traces examples in Supplementary Figs. 4 and 5). These slow kinetics are consistent with the long half-width duration of 9 s reported for myelin internodes in the neocortex [6]. It should be noted that the temporal resolution to detect some Ca<sup>2+</sup> events of OL lineage cells may require high acquisition rates (> 10 Hz), particularly at the level of myelin sheaths [6]. Although Occam's development was based on stacks acquired at rates between 1.75 Hz and 10 Hz, it properly process image stacks at high frequencies (40 Hz; Fig. 6h). In fact, Occam's performance is independent on the acquisition rate since the segmentation to detect active ROIs mainly depends on the quality of the projection images regardless the number of frames. Nevertheless, if Ca<sup>2+</sup> events are very brief, we recommend using

the 'miniscope configuration' as performed for simulations of objects changing location (Supplementary Fig. 2b-c). In addition, the user must define the parameters of the configuration file of post-prOccam according to the acquisition rate and the average kinetics of Ca<sup>2+</sup> events in order to adjust the post-processing to a fast acquisition condition (see Supplementary files).

In the present study, Occam was able to perform ROI detection and bleaching correction not only in two-photon imaging, but also in ex vivo and in vivo wide-field imaging conditions that have a low signal-to-noise ratio. In addition, Occam performed analyses faster than GECIquant and AQUA, demanded low memory and disk space. We also demonstrated that our software could successfully detect independent fluctuating Ca<sup>2+</sup> signals in both the soma and the processes of OPCs and OLs, as well as in myelin sheaths, while not taking into account constant fluorescence. Notably, our programs can analyze various Ca<sup>2+</sup> indicators including GCaMP5, GCaMP6f, GCaMP6s, mGCaMP6s, GCaMP6m, FLUO-4-AM, mGCaMP7s and OGB-1. Together with the software's ability to analyze image stacks obtained in wide-field and two-photon microscopy at different magnifications and from different imaging devices, these results confirm the versatility and reliability of the software. Oligodendroglia from healthy control, pathological and Ca<sup>2+</sup> activity-stimulated conditions could be analyzed, emphasizing the wide applicability of our analytical workflow. Of note, since image processing is not exactly the same in the different configurations of Occam, we recommend that users test the different configurations to find the one that best handles their data.

In conclusion, the presented imaging data analytical software will aid future investigations into the role of OPC and OL Ca<sup>2+</sup> signaling. As such, it might contribute to the elucidation of Ca<sup>2+</sup>-related mechanisms implicated in OL lineage cell function and dysfunction which could be relevant to understand the myelination process in healthy and diseased conditions.

**Supplementary Information** The online version contains supplementary material available at <https://doi.org/10.1007/s00018-023-05065-3>.

**Acknowledgements** We thank the NeurImag platform and the animal facility of IPNP and their funding sources (Fédération pour la Recherche Médicale, Fondation Leducq). We would also like to thank Serge Charpak and Yannick Goulam for their help with the two-photon microscope, Callum White for his contribution to initial data analysis in Python and Anastassia Voronova for sharing the protocol for CPZ-induced demyelination. A particular thank to David Lyons and Philipp Braaker, Tim Czopka and Patricia Bispo, Dwight Bergles, Brad Zuchero, Amit Agarwal for sharing their Ca<sup>2+</sup> imaging data and allowing us to test our software capabilities in OPCs and OLs recorded with different Ca<sup>2+</sup> indicators and in different species and imaging conditions.

**Author contributions** D.A.M. and B. M-S. conducted the wide-field Ca<sup>2+</sup> imaging experiments. C.H. performed the two-photon Ca<sup>2+</sup>

imaging experiments and D.A.M. performed the in vivo microendoscopy  $\text{Ca}^{2+}$  imaging experiments. D.A.M., B. M-S., C.H. and M.C.A. designed the experiments and analysis. P.B., D.A.M., B. M-S wrote the FIJI/ImageJ plugin. M.C.A. and F.R. designed the Python software and F.R. wrote the code. D.A.M. and M.C.A. performed the data analyses and D.A.M., F.R. and M.C.A. wrote the manuscript. M.C.A supervised the project.

**Funding** This work was supported by grants from a subaward agreement from the University of Connecticut with funds provided by Grant No. RG-1612-26501 from National Multiple Sclerosis Society (NMSS), Fondation pour l'aide à la recherche sur la Sclérose en Plaques (ARSEP), Fondation pour la Recherche Médicale (FRM, EQU202103012626), ANR under the frame of the European Joint Programme on Rare Diseases (EJP RD, project no. ANR-19-RAR4-008-03) and ANR CoLD (ANR, ANR-20-CE16-0001-01). D.A.M. received a postdoctoral fellowship from Fondation pour la Recherche Médicale (FRM, project SPF202005011919) and a L'Oréal-UNESCO young talents award 2021 for women in science, B. M.-S. received a PhD fellowship from Université Paris Cité, and C.H. received a postdoctoral fellowship from ARSEP. M.C.A. and F.R. are CNRS (Centre National de la Recherche Scientifique) investigators.

**Availability of data and materials** The data generated and analyzed during this study are included in the manuscript and supplementary files. Occam and post-prOccam programs as well as all the software documentation and a full example of ex vivo wide-field imaging data are hosted at <https://gitlab.com/d5674/occam> and published under a Free Software GNU GPLv3 + license.

## Declarations

**Conflict of interest** The authors have declared that no competing interests exist.

**Ethical approval** All experiments followed European Union and institutional guidelines for the care and use of laboratory animals and were approved by both the French ethical committee for animal care of the University Paris Cité (Paris, France) and the Ministry of National Education and Research (Authorization N° 13093-2017081713462292).

**Consent for publication** All the authors have given consent for publication.

## References

1. Abiraman K, Pol SU, O'Bara MA, Chen G-D, Khaku ZM, Wang J, Thorn D, Vedia BH, Ekwegbalu EC, Li J-X, Salvi RJ, Sim FJ (2015) Anti-muscarinic adjunct therapy accelerates functional human oligodendrocyte repair. *J Neurosci* 35(8):3676–3688. <https://doi.org/10.1523/JNEUROSCI.3510-14.2015>
2. Agarwal A, Wu P-H, Hughes EG, Fukaya M, Tischfield MA, Langseth AJ, Wirtz D, Bergles DE (2017) Transient opening of the mitochondrial permeability transition pore induces microdomain calcium transients in astrocyte processes. *Neuron* 93(3):587–605.e7. <https://doi.org/10.1016/j.neuron.2016.12.034>
3. Arganda-Carreras I, Kaynig V, Rueden C, Eliceiri KW, Schindelin J, Cardona A, Sebastian Seung H (2017) Trainable Weka segmentation: a machine learning tool for microscopy pixel classification. *Bioinformatics* 33(15):2424–2426. <https://doi.org/10.1093/bioinformatics/btx180>
4. Balia M, Benamer N, Angulo MC (2017) A specific GABAergic synapse onto oligodendrocyte precursors does not regulate cortical oligodendrogenesis. *Glia* 65(11):1821–1832. <https://doi.org/10.1002/glia.23197>
5. Baraban M, Koudelka S, Lyons DA (2018)  $\text{Ca}^{2+}$  activity signatures of myelin sheath formation and growth in vivo. *Nat Neurosci* 21(1):1. <https://doi.org/10.1038/s41593-017-0040-x>
6. Bettefeld A, Popovic MA, de Vries SI, Kole MHP (2019) High-frequency microdomain  $\text{Ca}^{2+}$  transients and waves during early myelin internode remodeling. *Cell Rep* 26(1):1. <https://doi.org/10.1016/j.celrep.2018.12.039>
7. Björnstad DM, Åbjørnsbråten KS, Hennestad E, Cunen C, Hermansen GH, Bojarskaite L, Pettersen KH, Vervaeke K, Enger R (2021) Begonia-a two-photon imaging analysis pipeline for astrocytic  $\text{Ca}^{2+}$  signals. *Front Cell Neurosci* 15:681066. <https://doi.org/10.3389/fncel.2021.681066>
8. Cantu DA, Wang B, Gongwer MW, He CX, Goel A, Suresh A, Kourdougli N, Arroyo ED, Zeiger W, Portera-Cailliau C (2020) EZcalcium: open-source toolbox for analysis of calcium imaging data. *Front Neural Circuits* 14:25. <https://doi.org/10.3389/fncir.2020.00025>
9. Chua Y, Morrison A (2016) Effects of calcium spikes in the layer 5 pyramidal neuron on coincidence detection and activity propagation. *Front Comput Neurosci*. <https://doi.org/10.3389/fncom.2016.00076>
10. Cohen RI, Almazan G (1994) Rat oligodendrocytes express muscarinic receptors coupled to phosphoinositide hydrolysis and adenylyl cyclase. *Eur J Neurosci* 6(7):1213–1224. <https://doi.org/10.1111/j.1460-9568.1994.tb00620.x>
11. Fiore F, Alhalaseh K, Dereddi RR, Bodaleo Torres F, Çoban I, Harb A, Agarwal A (2023) Norepinephrine regulates calcium signals and fate of oligodendrocyte precursor cells in the mouse cerebral cortex. *Nat Commun* 14(1):8122. <https://doi.org/10.1038/s41467-023-43920-w>
12. Giovannucci A, Friedrich J, Gunn P, Kalfon J, Brown BL, Koay SA, Taxis J, Najafi F, Gauthier JL, Zhou P, Khakh BS, Tank DW, Chklovskii DB, Pnevmatikakis EA (2019) CaImAn: an open source tool for scalable calcium imaging data analysis. *Elife* 8:e38173. <https://doi.org/10.7554/eLife.38173>
13. Ingiosi AM, Hayworth CR, Harvey DO, Singletary KG, Rempel MJ, Wisor JP, Frank MG (2020) A role for astroglial calcium in mammalian sleep and sleep regulation. *Curr Biol* 30(22):4373–4383.e7. <https://doi.org/10.1016/j.cub.2020.08.052>
14. Iyer M, Kantarci H, Ambiel N, Novak SW, Andrade LR, Lam M, Münch AE, Yu X, Khakh BS, Manor U, Zuchero JB (2023) Oligodendrocyte calcium signaling sculpts myelin sheath morphology. *BioRxiv*. 2023.04.11.536299. <https://doi.org/10.1101/2023.04.11.536299>
15. Koizumi S (2010) Synchronization of  $\text{Ca}^{2+}$  oscillations: involvement of ATP release in astrocytes: astrocytic  $\text{Ca}^{2+}$  oscillations and neuronal activities. *FEBS J* 277(2):286–292. <https://doi.org/10.1111/j.1742-4658.2009.07438.x>
16. Krasnow AM, Ford MC, Valdivia LE, Wilson SW, Attwell D (2018) Regulation of developing myelin sheath elongation by oligodendrocyte calcium transients in vivo. *Nat Neurosci* 21(1):1. <https://doi.org/10.1038/s41593-017-0031-y>
17. Li J, Miramontes T, Czopka T, Monk K (2022) Synapses and  $\text{Ca}^{2+}$  activity in oligodendrocyte precursor cells predict where myelin sheaths form. *BioRxiv*. <https://doi.org/10.1101/2022.03.18.484955>
18. Lu TY, Hanumaihgari P, Hsu ET, Agarwal A, Kawaguchi R, Calabresi PA, Bergles DE (2023) Norepinephrine modulates calcium dynamics in cortical oligodendrocyte precursor cells promoting proliferation during arousal in mice. *Nat Neurosci*. <https://doi.org/10.1038/s41593-023-01426-0>

19. Marisca R, Hoche T, Agirre E, Hoodless LJ, Barkey W, Auer F, Castelo-Branco G, Czopka T (2020) Functionally distinct subgroups of oligodendrocyte precursor cells integrate neural activity and execute myelin formation. *Nat Neurosci* 23(3):363–374. <https://doi.org/10.1038/s41593-019-0581-2>
20. Maas DA, Angulo MC (2021) Can enhancing neuronal activity improve myelin repair in multiple sclerosis? *Front Cell Neurosci* 15:645240. <https://doi.org/10.3389/fncel.2021.645240>
21. Mozafari S, Starost L, Manot-Saillet B, Garcia-Diaz B, Xu YKT, Roussel D, Levy MJF, Ottoboni L, Kim KP, Schöler HR, Kennedy TE, Antel JP, Martino G, Angulo MC, Kuhlmann T, Baron-Van Evercooren A (2021) Multiple sclerosis iPS-derived oligodendroglia conserve their properties to functionally interact with axons and glia in vivo. *Sci Adv* 6(49):eabc6983. <https://doi.org/10.1126/sciadv.abc6983>
22. Ortiz FC, Habermacher C, Graciarena M, Houry P-Y, Nishiyama A, Nait-Oumesmar B, Angulo MC (2019) Neuronal activity in vivo enhances functional myelin repair. *JCI Insight*. <https://doi.org/10.1172/jci.insight.123434>
23. Otsu Y, Couchman K, Lyons DG, Collot M, Agarwal A, Mallet JM, Pfrieger FW, Bergles DE, Charpak S (2014) Calcium dynamics in astrocyte processes during neurovascular coupling. *Nat Neurosci* 18(2):210–218. <https://doi.org/10.1038/nn.3906>
24. Paez PM, Lyons DA (2020) Calcium signaling in the oligodendrocyte lineage: regulators and consequences. *Annu Rev Neurosci* 43:163–186. <https://doi.org/10.1146/annurev-neuro-100719-093305>
25. Pitman KA, Young KM (2016) Activity-dependent calcium signalling in oligodendrocyte generation. *Int J Biochem Cell Biol*. <https://doi.org/10.1016/j.biocel.2016.05.018>
26. Sahel A, Ortiz FC, Kerninon C, Maldonado PP, Angulo MC, Nait-Oumesmar B (2015) Alteration of synaptic connectivity of oligodendrocyte precursor cells following demyelination. *Front Cell Neurosci* 9:77–77. <https://doi.org/10.3389/fncel.2015.00077>
27. Schindelin J, Arganda-Carreras I, Frise E, Kaynig V, Longair M, Pietzsch T, Preibisch S, Rueden C, Saalfeld S, Schmid B, Tinevez J-Y, White DJ, Hartenstein V, Eliceiri K, Tomancak P, Cardona A (2012) Fiji: an open-source platform for biological-image analysis. *Nat Methods* 9(7):676–682. <https://doi.org/10.1038/nmeth.2019>
28. Thevenaz P, Ruttimann UE, Unser M (1998) A pyramid approach to subpixel registration based on intensity. *IEEE Trans Image Process* 7(1):27–41. <https://doi.org/10.1109/83.650848>
29. Venugopal S, Srinivasan R, Khakh BS (2019) GECIquant: semi-automated detection and quantification of astrocyte intracellular Ca<sup>2+</sup> signals monitored with GCaMP6f. In: De Pittà M, Berry H (eds) *Computational glioscience*. Springer International Publishing, Berlin, pp 455–470. [https://doi.org/10.1007/978-3-030-00817-8\\_17](https://doi.org/10.1007/978-3-030-00817-8_17)
30. Wang Y, DelRosso NV, Vaidyanathan TV, Cahill MK, Reitman ME, Pittolo S, Mi X, Yu G, Poskanzer KE (2019) Accurate quantification of astrocyte and neurotransmitter fluorescence dynamics for single-cell and population-level physiology. *Nat Neurosci* 22(11):1936–1944. <https://doi.org/10.1038/s41593-019-0492-2>
31. Welliver RR, Polanco JJ, Seidman RA, Sinha AK, O'Bara MA, Khaku ZM, Santiago González DA, Nishiyama A, Wess J, Feltri ML, Paez PM, Sim FJ (2018) Muscarinic receptor M<sub>3</sub>R signaling prevents efficient remyelination by human and mouse oligodendrocyte progenitor cells. *J Neurosci* 38(31):31. <https://doi.org/10.1523/JNEUROSCI.1862-17.2018>
32. Xu YKT, Call CL, Sulam J, Bergles DE (2021) Automated in vivo tracking of cortical oligodendrocytes. *Front Cell Neurosci* 15:667595. <https://doi.org/10.3389/fncel.2021.667595>
33. Yuan T, Lu J, Zhang J, Zhang Y, Chen L (2015) Spatiotemporal detection and analysis of exocytosis reveal fusion “hotspots” organized by the cytoskeleton in endocrine cells. *Biophys J* 108(2):251–260. <https://doi.org/10.1016/j.bpj.2014.11.3462>

**Publisher's Note** Springer Nature remains neutral with regard to jurisdictional claims in published maps and institutional affiliations.

Springer Nature or its licensor (e.g. a society or other partner) holds exclusive rights to this article under a publishing agreement with the author(s) or other rightsholder(s); author self-archiving of the accepted manuscript version of this article is solely governed by the terms of such publishing agreement and applicable law.